Cooperative antagonistic mechanism driven by bidirectional pneumatic artificial muscles for soft robotic joints☆

Jae Hyeong Park, Kihyeon Kim, Young Jin Gong, Sang Yul Yang, Seong Taek Hwang, Ho Sang Jung, Hyungpil Moon, Ja Choon Koo, Hugo Rodrigue, Hyouk Ryeol Choi *

School of Mechanical Engineering, Sungkyunkwan University, 2066, Seobu-ro, Jangan-gu, Suwon-si, 16419, Gyeonggi-do, Republic of Korea

ARTICLE INFO

ABSTRACT

Actuators and mechanisms are the most important components of soft robots. In this study, we introduce a novel actuator capable of bidirectional force transmission, and an antagonistic structural pair mechanism that can cooperate with actuators. A tendon that runs through the interior of the actuator allows bidirectional force transmission. Each contraction and expansion can produce 124.46 N and 122.80 N of force, and maximum contraction and expansion ratios of 75.1% and 402.1%, respectively. However, a cooperative antagonistic mechanism that can transmit force in the pushing direction using a soft frame and a closed-loop tendon has also been developed. Remarkably, it exhibits 2.58 times the lumped torque density compared to a traditional antagonistic mechanism. When integrated into a robotic arm, this mechanism enables the arm to lift a 2 kg object by 117° on a 30 cm moment arm. The robotic arm itself is efficiently designed, with a 340 mm upper arm and a 300 mm forearm, maintaining a lightweight structure at just 380 g.

1. Introduction

To date, robots have been used primarily in manufacturing facilities. More recently, the use of robots in daily life has gradually increased. Robots will soon be expected to share living spaces, collaborate, and provide various services to humans. Traditional robots, consisting of electrical or hydraulic motors, are unsatisfactory in terms of weight, power, safety, and price for such applications [1]. Therefore, research is required to produce better actuators and appropriate power transfer mechanisms. Many researchers have studied lightweight, high-performance, safe, and low-cost artificial muscles, and soft robots as alternatives to conventional robots [2,3]. Various artificial muscles have been studied to create linear motion, such as human muscles, and use this linear motion to create rotational joints. Artificial muscles typically include the following actuator types—shape memory alloy [4,5], twisted and coiled [6–9], twisted string [10], dielectric elastomer [11,12], and pneumatic.

Pneumatic actuators have more practical applications than other artificial muscles because they can produce large forces and strains. The McKibben muscle [13–15], for example, can create a large force using high-pressure levels, but it has a contraction ratio of 30%.

To address these limitations, researchers have explored various structural modifications. Actuators employing origami or bellows structures, for instance, leverage these designs to achieve a higher contraction ratio, as evidenced by multiple studies [16–22]. Folding-type actuators, on the other hand, showcase the capability to fully fold, thus achieving a substantial expansion ratio [23–26].

The inherent challenge with these actuators is their unidirectional movement. In human musculoskeletal systems, bidirectional movement is a result of the combined action of agonists and antagonists. Replicating this in artificial systems traditionally requires two actuators in an antagonistic setup. While this does achieve the desired bidirectional movement, it increases the space requirement and complexity. Efforts have been made to achieve bidirectional motion by linking antagonistic structures [20,23,25,27–29] and soft actuators [30,31]. However, these configurations rely on two distinct actuators, leading to spatial inefficiencies.

Our research marks a notable advance in this domain. We introduce an actuator capable of bidirectional movement, addressing the spatial challenges of traditional dual-actuator setups. While there are existing studies on bidirectional pneumatic artificial muscles, they often compromise on force and strain [32,33]. Our research to overcome these
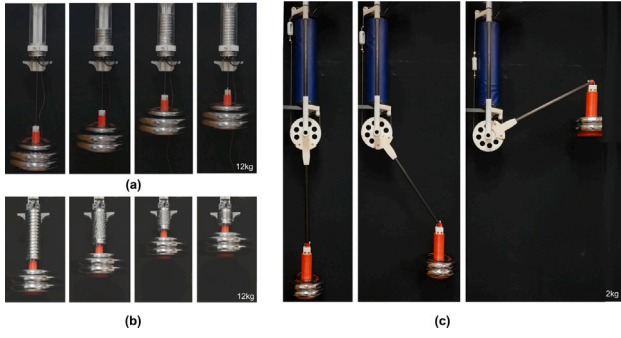

Fig. 1. (a) Expansion of the BiPAM with 12 kg payload at 80 kPa. (b) Contraction of the BiPAM with 12 kg payload at −70 kPa. (c) Lifting of the CoAM with 2 kg payload at the end effector with depressurization and pressurization.

limitations and provides a new solution to a long-standing challenge in compressed air actuator design.

This study introduces a novel pneumatic artificial muscle and a mechanism to address these problems (Fig. 1 and Video 1). This study introduces a novel pneumatic artificial muscle called Bidirectional Pneumatic Artificial Muscles (BiPAM), which can actively generate contractile and expansion forces. They can be used individually or in pairs as Dual-Chamber BiPAMs (DC-BiPAM). The BiPAMs can generate contractile forces of up to 122.80 N and expansion forces of up to 124.46 N. The study also highlights the Cooperative Antagonistic Mechanism (CoAM), a unique structure that increases volumetric efficiency and enables force transfer to joints. The CoAM demonstrated 2.58 times greater volumetric efficiency compared to conventional structures. The design, fabrication processes, force characteristics, and dynamic response of BiPAMs are described in Section 2, while the operating principles and quasi-static models of CoAM are explained in Section 3. The experimental results are presented and discussed in Sections 4 and 5. These innovations differentiate BiPAMs and CoAM from other actuators, emphasizing their unique capabilities in active bidirectional motion and high torque generation through cooperative actuation.

2. Bidirectional pneumatic artificial muscle

2.1. Actuator design and operating principle

The configuration of a BiPAM is shown in Fig. 2(a). The BiPAM is an air chamber comprising an bellows (SUNJU AIRTECH, A.L D50) and an inner deformable structure, and two sealing caps that prevent air from flowing in. The bellows have a metal wire spirally wound on the outside, and the surface is composed of a thin film of aluminum. Therefore, it can be easily folded and unfolded in the longitudinal direction without shrinking in the circumferential direction. Two sealing caps were 3D-printed (VeroWhite). The top of the inner structure was open and exposed to outside air, and the bottom was blocked by the bottom cap. The top cap has a hole in its center, to enable its assembly with the inner cylinder. An air-fitting is fixed onto the top cap slightly off-center, to enable the pressure inside the chamber to be controlled through an air tube.

The bottom cap comprises the portion that transmits the force of the actuator, which enables the upper and lower sides of this portion to be connected to the tendon. Because an axial deformable fabric structure was used, it was possible to transfer the force from the underside of the actuator through a connected tendon without air leakage. By regulating the BiPAM chamber pressure, bidirectional movement, and force transfer could be achieved. By depressurizing or pressurizing the actuator, the bellows are folded or unfolded to contract or expand in the longitudinal direction of the actuator. If the top cap of the
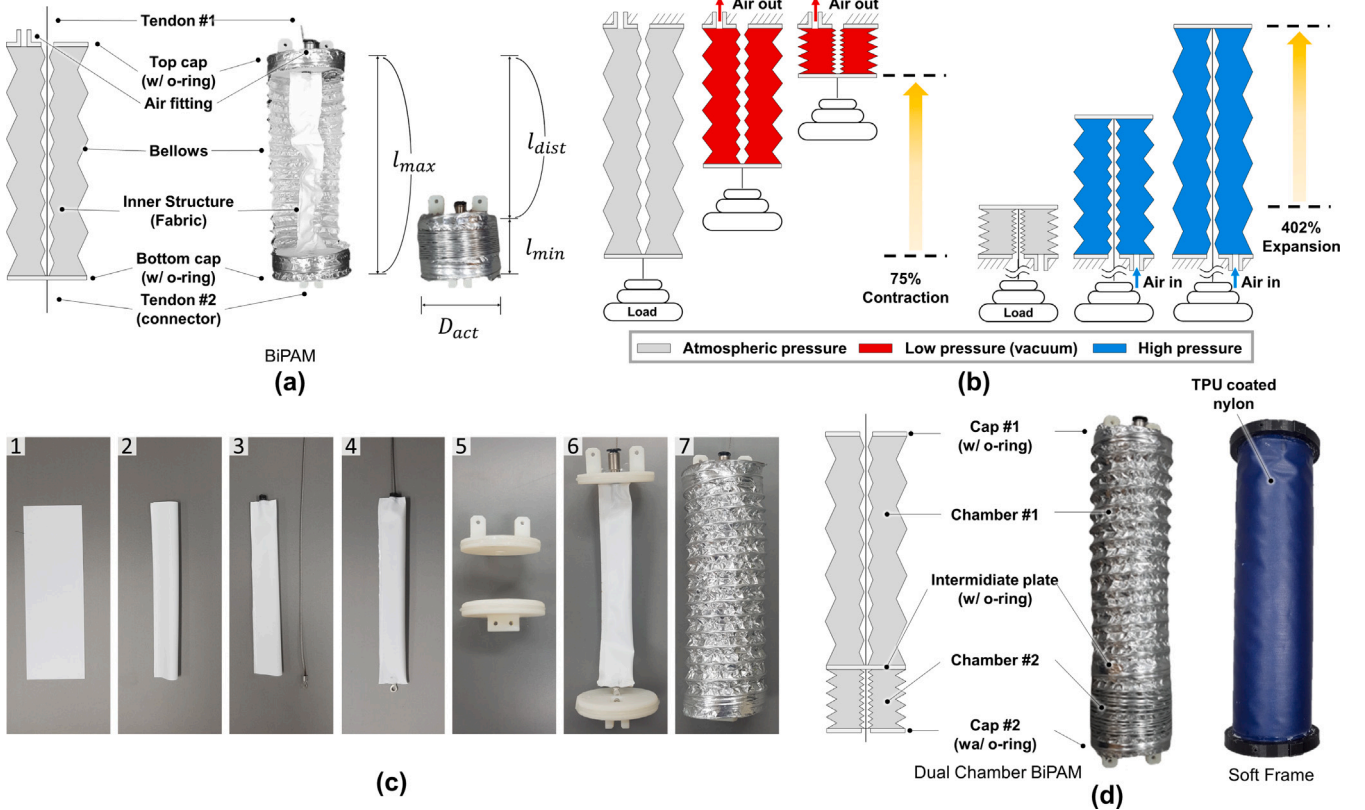

Fig. 2. (a) Configuration of the BiPAMs (cross-sectional view). (b) Operating principle of the BiPAMs. (c) The fabrication process of the BiPAMs. (d) Configuration of the DC-BiPAMs and Soft frame.

Table 1
Comparison of other foldable PAMs.

Actuator	Actuating type	Max. cross-sectional area (mm^2)	Actuator length (mm)	Payload (kg)	Displacement (mm)	Lumped work density (J/mm^3)
OVPAM [21]	Contraction	3.50×10^3	90	8	89.73	22.31×10^{-6}
Plant-inspired [23]	Expansion	0.23×10^3	250	0.4	190	13.13×10^{-6}
APAM [26]	Contraction, Expansion	2.03×10^3	130	0.5^a	120.9	2.25×10^{-6}
DC-BiPAM (This work)	Contraction, Expansion	2.51×10^3	216	24 (12 each)	130	56.29×10^{-6}

^{a} The expansion payload of APAM is excluded because there is no data in the longitudinal direction.

BiPAM is secured to an external frame such as the ceiling, the payload is hung on the bottom cap. Subsequently, the inside of the actuator is decompressed, and it can be loaded by contraction. This can also be achieved by securing the top cap of the actuator to the same outer frame as the floor, connecting a tendon across the central fabric structure to the bottom cap of the actuator, attaching the payload to it, and pressurizing the inside of the actuator (Fig. 2(b)).

When examining the designs of various actuators in detail, clear distinctions become evident. The OVPAM [21] is characterized by its external origami structure and contracts by depressurizing its internal chamber. In contrast, the Plant-inspired actuator [23] features a chamber wrapped in fabric with a tendon in the center; it expands upon pressurizing this inner chamber. The APAM [26] is designed with an internal chamber within the cylindrical structure and another chamber that wraps around its exterior. While APAM supports bidirectional operation, its movement is not through expansion, primarily serving as a brace, and due to its low operating pressure, it cannot lift heavy weights. Contrarily, BiPAM, although composed of a single chamber, can be perceived as a fusion of the principles behind both the OVPAM [21] and the Plant-inspired [23]. This combination allows BiPAM to not only move in both directions but also lift substantial weights. (Figs. 1(a) and 1(b))

2.2. Fabrication process

Actuator fabrication is explained as follows (Fig. 2(c)).

1. The fabric is cut into rectangular pieces.
2. Each piece is folded once along the horizontal direction, and the facing longitudinal edges are sealed using heat adhesion to create a cylindrical shape.
3. A tube that fits the central hole is cut to the appropriate length and attached to the adhesive. Subsequently, a flexible wire (Sava cable, 2047) is connected with a crimping terminal attached to the end.
4. A flexible wire is inserted into the cylindrical fabric and an adhesive is used to attach the bottom cap to the crimping terminal.
5. O-rings are inserted into the top and bottom caps.
6. The hole of the upper cap is glued to the tube of the fabric cylinder and assembled with the bottom cap, into which the compression terminal and O-rings are inserted with bolts.
7. The bellows are covered, and the top and bottom caps are glued and sealed

The fabricated prototype of the actuators had a diameter, D_{act}, of 56.6 mm. The distance between the top and bottom caps (l_{dist}) is 130 mm, the maximum length (l_{max}) is 173 mm, and the minimum length of the BiPAMs (l_{min}) is 43 mm. According to Eqs. (1) and (2), contraction and expansion increased to 75.1% and 402.3%, respectively. ϵ_{con} and ϵ_{exp} are contractile and expandable strains, respectively.

$$\epsilon_{con} \; [\%] = \frac{l_{dist}}{l_{max}} \times 100 \tag{1}$$

$$\epsilon_{exp} \; [\%] = \frac{l_{max}}{l_{min}} \times 100 \tag{2}$$

2.3. Dual chamber BiPAM

Soft linear actuators have varying lengths, which means they possess both minimum and maximum possible volumes. When using these actuators in a robot, one often needs to allocate as much space as the maximum volume requires, which is not space-efficient. BiPAM encounters the same dilemma. However, given that BiPAM has a structure surrounding the tendon, this issue can be addressed by connecting two BiPAMs in series.

Although it is possible to use two BiPAMs connected, in this study, a DC-BiPAM was manufactured and used to shorten the manufacturing time and reduce the space of one bottom cap. As shown in Fig. 2(d), the DC-BiPAM is composed of a cap #1, an intermediate plate, and a cap #2. Chambers #1 and #2 were separated using an intermediate plate. Because the DC-BiPAMs have bidirectional motion and collaborate with other BiPAMs, DC-BiPAM shows better volumetric efficiency than the other existing folding pneumatic actuators. By utilizing a cylindrical soft frame made of TPU coated nylon fabric, buckling phenomena during the expansion operation of DC-BiPAM can be effectively prevented. To compare the study with the folding actuators of other researchers, we define the lumped work density, which is shown in Eq. (3)

$$\text{Lumped Work Density} = \frac{W_{act}}{V_{act}} = \frac{F_{payload} \cdot x_{act}}{A_{cross} \cdot l_{max}} \tag{3}$$

A_{cross} is the cross-sectional area of the actuators, V_{act} is the maximum occupied volume of the actuator, $F_{payload}$ is the force caused by the payload, and W_{act} is actuator work. The work of the actuator compared to the maximum volume occupied by the actuator is summarized in the lumped work density and compared in Table 1. BiPAM payload is 12 kg in both directions (Fig. 1). Thus, lumped work density of DC-BiPAM is 56.29 kJ/m^3, which showed the best volumetric efficiency.

2.4. Control system for experiment

To control the pressure of the BiPAMs, a pneumatic circuit was constructed, as shown in Fig. 3. Positive pressure was supplied to the air compressor (SAMJIN ENG) and controlled by pneumatic regulators (ITV-2030). The vacuum generator (SCPSi-L HV 3-20 NC M12-5) received a positive pressure from the air compressor to generate a negative pressure, and the output of this negative pressure was controlled by vacuum regulators (ITV-2090). Ports 1 and 2 were configured to maintain constant pressure inside the actuator, and ports 3 and 4 were configured to switch positive/negative pressure using a 5-port 3-position valve (VUVG-L10-P53C- ZT-M5-1P3). The pneumatic regulators, vacuum generator, and 5-port 3-position valve were controlled by the LabVIEW program on the host computer with analog signals from the data acquisition device (NI-cRIO). The block diagram for port 3 is shown in Fig. 3(b). When the target displacement is set, the error value is calculated by comparing it with the current displacement, and the PWM value is calculated through the PI controller. The sign of the PWM determines the direction of the pressure of the 5-port 3-position valve, and the absolute value of the PWM determines the magnitude of the pressure through the vacuum/positive regulator and is exported to BiPAM.
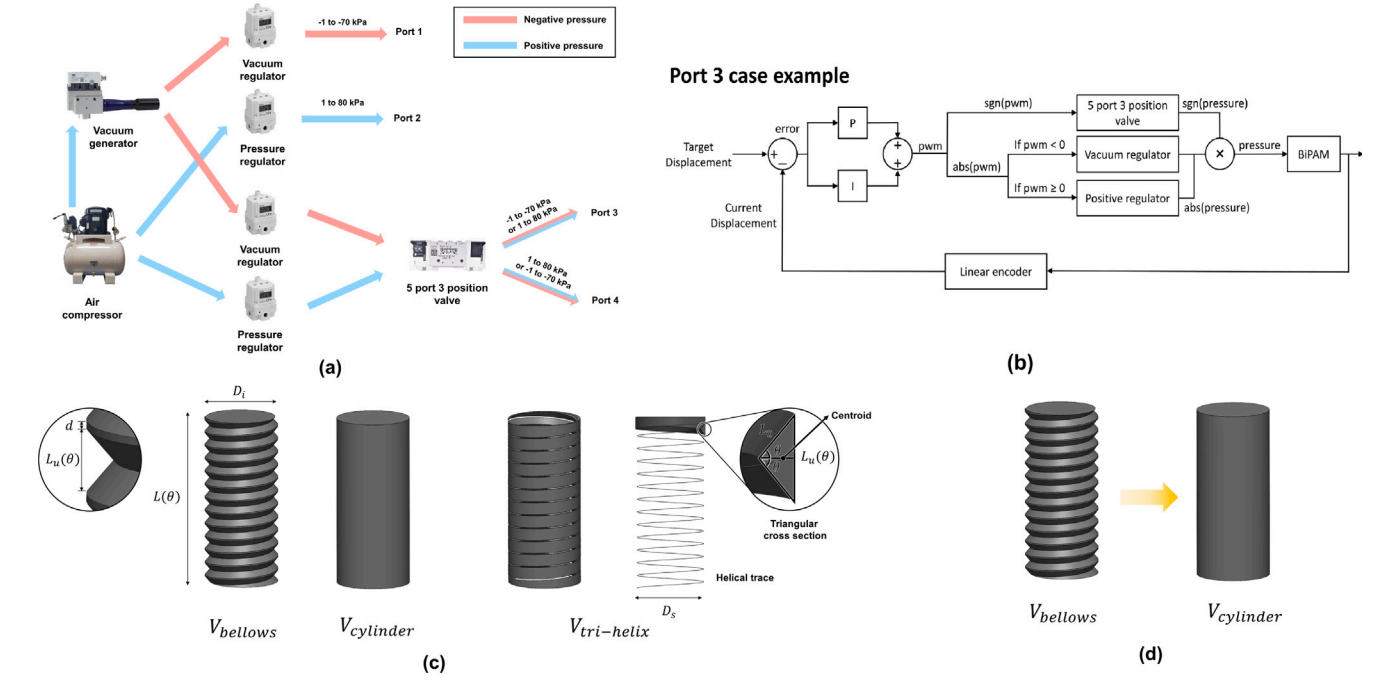
Fig. 3. (a) Pneumatic circuit diagram. (b) Block diagram of Port 3 case. (c) The volume of bellows. (d) Bellows change when pressurizing the BiPAM.

2.5. Quasi-static model of BiPAM

The force of the BiPAM was analyzed using a quasi-static model. The following equation can be obtained by work equilibrium and chain rule [34].

$$F dL = -P dV \tag{4}$$

$$F(\theta) = -P \frac{dV}{dL} = -P \frac{\frac{dV}{d\theta}}{\frac{dL}{d\theta}} \tag{5}$$

In case of contraction, As the pressure is reduced, the bellows of the entire length, $L(\theta)$, are contracted uniformly. D_i is internal diameter of BiPAM. The volume of the bellows, $V_{bellows}$, is equal to the volume of the cylinder, $V_{cylinder}$, minus the trace of the volume, $V_{tri-helix}$, moving along the spiral curve in the triangular cross-section. $V_{tri-helix}$ is equal to the product of the triangle area and the length of its centroid trace [35].

$$V_{bellows} = V_{cylinder} - V_{tri-helix} \tag{6}$$

$$V(\theta) = \frac{\pi D_i^2}{4} \cdot L - A \cdot l_{arc} \tag{7}$$

Following equations are obtained from the triangular cross-section in Fig. 3(c).

$$L(\theta) = n(L_u + d) \tag{8}$$

$$L_u(\theta) = 2L_0 \sin \theta \tag{9}$$

$$A(\theta) = \frac{1}{2} L_0^2 \sin 2\theta \tag{10}$$

D_s is The diameter of the spiral curve, the distance between the centroid and centroid of the triangle. l_{arc} is the length of the curve through the centroid of the triangle.

$$D_s(\theta) = D_i - \frac{1}{3} L_0 \cos \theta \tag{11}$$

$$l_{arc}(\theta) = 2n\pi \sqrt{\left(\frac{D_s}{2}\right)^2 + \left(\frac{L_u}{2\pi}\right)^2} \tag{12}$$

Eq. (13) can be obtained by differentiating Eq. (7) concerning the θ. By substituting Eqs. (8) and (13) into (5), Eq. (14), which is the

contractile force of BiPAM, can be obtained.

$$\frac{dV}{d\theta} = \frac{n\pi D_i^2}{4} \cdot \frac{dL_u}{d\theta} - \frac{dA}{d\theta} \cdot l_{arc} - A \cdot \frac{dl_{arc}}{d\theta} \tag{13}$$

$$F_{con,model}(\theta) = -P \frac{\frac{n\pi D_i^2}{4} \cdot \frac{dL_u}{d\theta} - \frac{dA}{d\theta} \cdot l_{arc} - A \cdot \frac{dl_{arc}}{d\theta}}{n \frac{dL_u}{d\theta}} \tag{14}$$

Eq. (14) relates the force on the actuator to the pressure being depressurized, and includes a term related to the actuator's geometry, the ratio of the change in volume to the change in length (dV/dL). The force is directly proportional to the pressure, while the term accounts for the mechanical deformation caused by the pressure difference, which affects the force the actuator can generate.

When the actuator is pressurized, the inside air pushes the folded part of the bellows outward, and the bellows shape changes to a cylindrical shape as shown in Fig. 3(d). In the case of a cylinder, dV/dL is the cross-sectional area of a circle, so it can be expressed as an Eq. (15).

$$F_{exp,model} = P \frac{\pi D_i^2}{4} \tag{15}$$

Eq. (15) shows that the force generated when pressing down on an actuator is proportional to the internal pressure, regardless of how the actuator's geometry changes.

2.6. Force characteristics of BiPAM

Experiments were conducted by dividing the contraction and expansion statuses. In both experiments, the displacement was initially set to 0 mm, based on the scenario in which the structure of the bellows is folded. In the contraction experiment, the top cap was fixed to the outer frame and a load cell (CZL601, 20 kg) was connected to the end. As the bottom cap could be moved freely, the length of the actuator was adjusted from 25 to 125 mm in five increments of 25 mm each (Fig. 4(a)). The pressure was reduced in 10 kPa steps from −10 kPa to −50 kPa through port 1. The experiment was performed in five steps: The actuator could produce a maximum force of 124.46 N when the length was 125 mm and the internal pressure was −50 kPa.
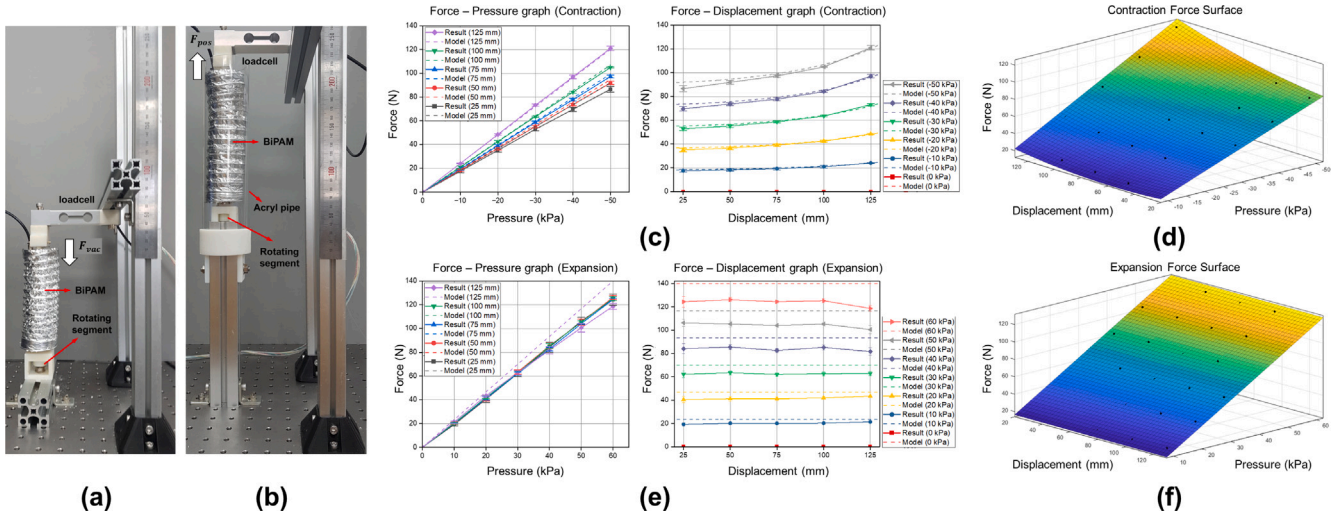
Fig. 4. (a) Blocked force experimental setup of contraction. (b) Blocked force experimental setup of expansion. (c) Characteristics of the BiPAMs when depressurized. (d) Contraction force fitting using MATLAB. (e) Characteristics of the BiPAMs when pressurized. (f) Expansion force fitting using MATLAB.

Table 2
Measured values of BiPAM.

Parameter	Value
θ	50° to 0°
d	1 mm
L_0	6 mm
D_i	54.5 mm
n	14 turns

Table 3
Coefficient table of BiPAM characteristics.

Coefficient	Value	Coefficient	Value
c_{00}	6.372	e_{00}	−0.8884
c_{10}	−0.2148	e_{10}	0.01138
c_{01}	−1.517	e_{01}	2.077
c_{11}	−0.001426		
c_{20}	0.00656		

When the pressure is less than that, the inner structure expands inside the bellows, causing frequent tearing. The force–pressure and force–displacement graphs are shown in Fig. 4(c). Dashed lines are calculated data from Eq. (14) with measured data (Table 2). At the same displacement, the force–pressure graph shows a linear tendency as the pressure inside the actuator changes. The force–displacement graph shows that the tendency of the force is similar to that of a second-order polynomial, depending on the displacement of the actuator at the same pressure. To precisely get the relationship between the force–pressure graph and the displacement of the BiPAMs based on the experimental data, a MATLAB curve fitting tool is used (Fig. 4(d)). This relational expression is shown in Eq. (16), where F_{con} represents the force of the BiPAM when it contracts, x_{con} represents the displacement of the actuator during contraction as a positive value, and P_{vac} represents the pressure difference between the actuator and atmospheric pressure as a positive value.

In the expansion experiment, the top cap was fixed to the outer frame and connected to the load cell at the end of the bottom cap, which could be moved freely, and the actuator length was changed from 25 to 125 mm in five 25 mm increments (Fig. 4(b)). The pressure inside the actuator in each step was controlled by port 2, and the experiment was performed in six steps by changing the pressure from 10 to 60 kPa. During the experiment, a transparent acrylic pipe was installed outside the actuator to prevent buckling. When the displacement of the actuator was 100 mm and the internal pressure was

60 kPa, the maximum force was 122.80 N. The force–pressure and force–displacement graphs are shown in Fig. 4(e). Dashed lines are calculated data from Eq. (15) with measured data (Table 2). At the same displacement, the force–pressure graph shows that is linear as the pressure inside the actuator changes. The force–displacement graph shows that there is no significant change in the displacement of the actuator at the same pressure. To precisely get the relationship between the force, pressure, and length of the actuator based on the experimental data for the expansion force, a MATLAB curve-fitting tool was used (Fig. 4(f)). This relational expression is shown in Eq. (17), where F_{exp} represents the force of the BiPAM when it expands, x_{exp} represents the displacement of the actuator during expansion as a positive value, and P_{pos} represents the pressure difference between the actuator and atmospheric pressure as a positive value. Coefficients of Eqs. (16) and (17) are in Table 3.

$$F_{con} = c_{00} + c_{10}x_{con} + c_{01}P_{vac} + c_{11}x_{con}P_{vac} + c_{20}x_{con}^2 \quad (16)$$

$$F_{exp} = e_{00} + e_{10}x_{exp} + e_{01}P_{pos} \quad (17)$$

2.7. Dynamic response

For the dynamic characteristic experiment of the actuator, the experimental equipment was constructed as shown in Figs. 5(a) and 5(b). In the experiment, the actuator was controlled using a PI controller (Kp = 1.1, Ki = 0.02). Port 3 was connected to the actuator. If the value obtained by subtracting the current pressure from the target pressure was negative, the positive pressure was positive, and if the value was positive, the negative pressure was switched to the 5-port 3-position valve. The displacement of the actuator was measured using a linear encoder (LM10IC020BB10A00). To check the maximum speed of the actuator, 91 mm (corresponding to 70% of the actuator displacement) was provided as a step input. The maximum speed was measured based on the rising time. The experimental setup shown in Fig. 5(a) was used for contraction experiments. Because the rising time was 1.25 s and the displacement was 72.8 mm, the speed was 58.24 mm/s (Fig. 5(c)). The experimental setup shown in Fig. 5(b) was used for the expansion experiments. Because the rising time was 0.85 s and the displacement was 72.8 mm, the speed was 85.17 mm/s (Fig. 5(d)). Using port 3 as the experimental setup in Fig. 5(a), the amplitude 0–13 mm (10% of the actuator displacement) sine response increases from 0.2 Hz to 2.2 Hz in 0.2 Hz increments. The bandwidth with a magnitude of −3 dB is approximately 2.1 Hz, and as the driving frequency increases, the phase increases.
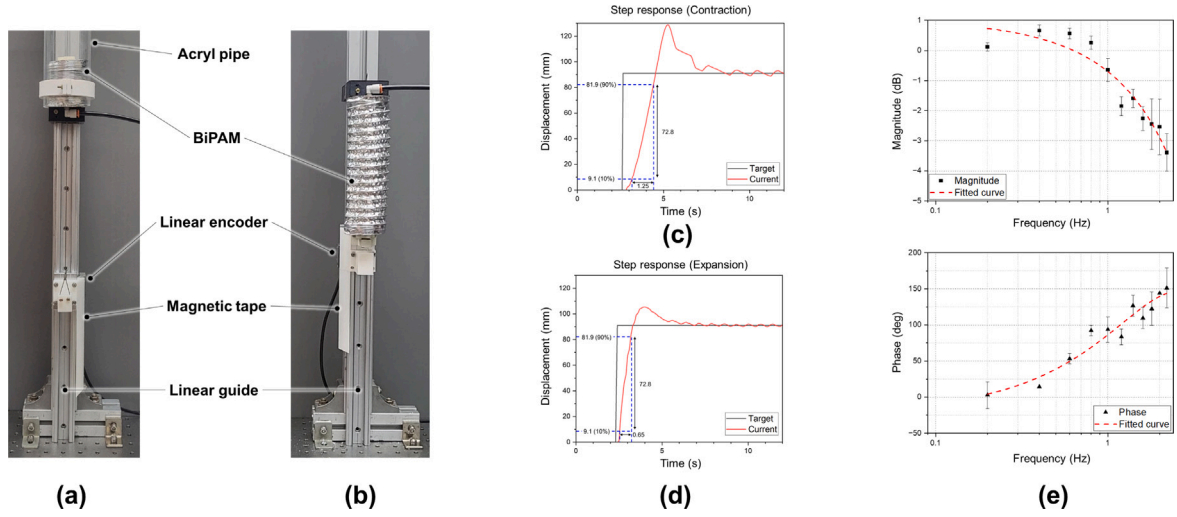
Fig. 5. (a) Dynamic response experimental setup of contraction. (b) Dynamic response experimental setup of expansion. (c) step response of contraction (d) step response of expansion (e) sinusoidal response of the BiPAMs.
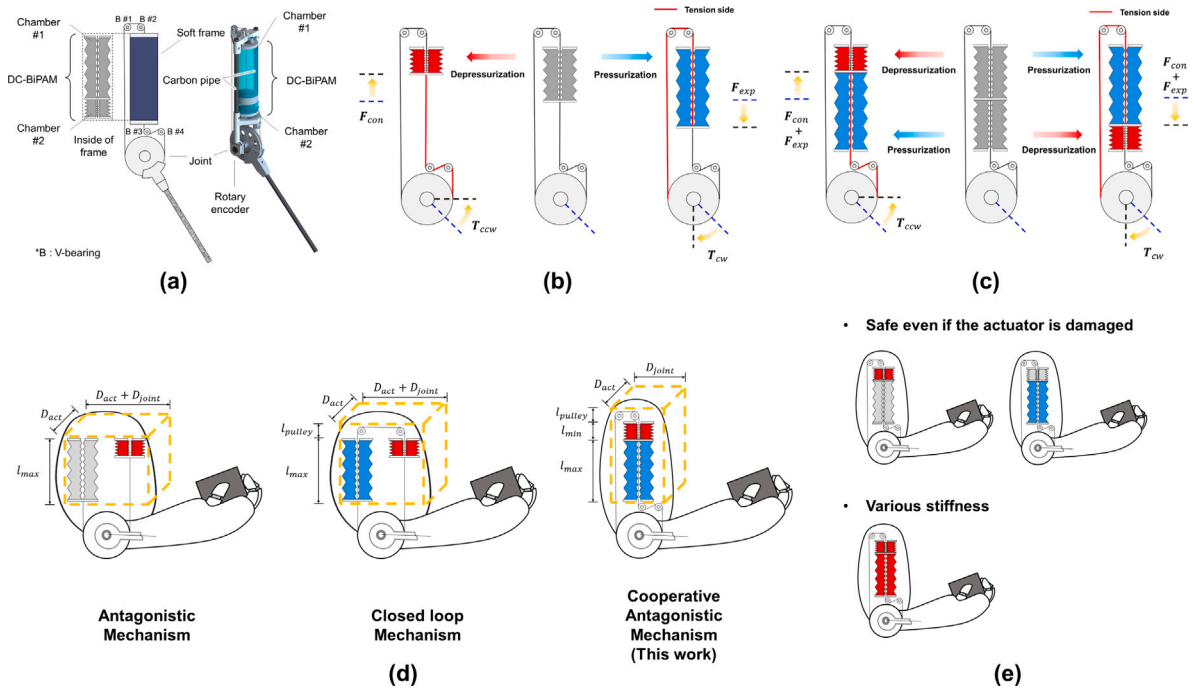

Fig. 6. (a) Schematic and 3D modeling of CoAM. (b) Operating principle of bidirectional robotic joint with a single BiPAM. (c) Operating principle of a CoAM with a DC-BiPAM. (d) Three different mechanisms driven by BiPAM. (e) Additional advantages of the CoAM.

3. Co-operative antagonistic mechanism

3.1. Mechanism design

The CoAM is a rotational mechanism that uses a bidirectional soft linear actuator. This mechanism can be implemented using either a single BiPAM or a DC-BiPAM that actuates cooperatively. Fig. 6(a) shows the overall configuration. The CoAM comprises an actuator, a tendon that transmits the force of the actuator, four bearings for tendon routing, and a rotating joint. When the actuator expands, the tendon loosens and cannot transmit force. Therefore, by configuring the tendon as a closed loop, it can be pulled inside the expanding actuator to enable force transmission, even if the actuator expands. To solve the buckling problem that may occur during pressurization, a cylindrical soft frame made of nylon fabric was attached. The intermediate plate

of the DC-BiPAM has a tendon connected in both the upward and downward directions. When the tendon is connected to the upward direction of the intermediate plate, bearing 1 changes the direction of the force of the upper tendon, and bearing 2 changes the force of the actuator to be parallel to the actuator and tangential to the pulley to generate a joint torque. When the tendon is connected to the downward direction of the intermediate plate, it is not necessary to change the direction of the force because the tendon uses a contraction force. However, the force was changed to be parallel to the actuator, and the tendon was connected to the joint diagonally through bearings 3 and 4 to make the force tangential to the pulley.

3.2. Bidirectional robotic joint with single BiPAM

The mechanism that is driven by a single BiPAM, and its operating principle, is shown in Fig. 6(b). When the BiPAM contracts by

Table 4
Parameters of work density comparison.

Mechanism	Exerted force	Volume (mm^3)	Torque (N·m)	Lumped torque density (N·m/mm^3)	Lumped torque density (relative)
Antagonistic Mechanism	F_{con}	1.34×10^6	3.98	2.98×10^{-6}	1
Closed loop Mechanism	F_{con}, F_{exp}	1.65×10^6	8.91	5.41×10^{-6}	1.82
Co-operative Antagonistic Mechanism (This work)	F_{con}, F_{exp}	1.16×10^6	8.91	7.69×10^{-6}	2.58

depressurization, the force of the tendon connected to its bottom cap is transmitted to the joint through bearings 3 and 4. This causes the joint to rotate in the counterclockwise (CCW) direction. Conversely, when the actuator is inflated by pressurization, the force of the tendon connected to the bottom cap of the actuator is transmitted to the joint through bearings 1 and 2. The resulting torque causes the joint to rotate in the clockwise (CW) direction. Therefore, this mechanism enables the bidirectional rotational movement with a single actuator by adjusting the internal pressure of the actuator to decrease or increase.

3.3. CoAM with DC-BiPAM

The mechanism that is driven by a DC-BiPAM, and its operating principle, are shown in Fig. 6(c). Caps #1 and #2 are fixed to the frame to which the carbon pipe is connected. The intermediate plate transmits the force of the DC-BiPAM. The caps #1 and #2 are the fixed parts, and the intermediate plate is the movable part. When chamber #1 is depressurized and chamber #2 is pressurized simultaneously, chamber #1 contracts and chamber #2 expands. Therefore, the movable part moves upward owing to the force generated by both chambers. When the movable part moves upward, the tension in the tendon causes the joint to rotate in CCW. Conversely, if chamber #1 is pressurized while chamber #2 is depressurized, the joint rotates CW and the movable part moves downward by both chambers.

The main advantage of the CoAM over the conventional mechanism is its volumetric efficiency. To demonstrate this, our group chose three mechanisms. An antagonistic mechanism (AM), a closed loop mechanism (CLM), and a CoAM (Fig. 6(d)). AM is a mechanism in which a unidirectional actuator drives in opposite directions. A CLM is a mechanism in which the ends of the actuators are connected by tendons so that the bidirectional actuators can cooperate or move in opposite directions. The CoAM is the mechanism proposed in this study. Our group defines lumped torque density as the torque divided by the occupying volume, as shown in Eq. (18).

$$\text{Lumped Torque Density} = \frac{T_i}{V_i} (i = \text{AM,CLM,CoAM}) \quad (18)$$

The volume occupied by the actuator for each mechanism configuration is as follows: In this study, it was assumed that the volume occupied by the bidirectional actuator when it was placed inside the robot was a cuboid

$$V_{AM} = (D_{act} + D_{joint}) \cdot l_{max} \cdot D_{act} \quad (19)$$

$$V_{CLM} = (D_{act} + D_{joint}) \cdot (l_{max} + l_{pulley}) \cdot D_{act} \quad (20)$$

$$V_{CoAM} = D_{joint} \cdot (l_{max} + l_{min} + l_{pulley}) \cdot D_{act} \quad (21)$$

D_{joint} is the diameter of the joint and l_{pulley} is the height of the volume occupied by the pulley.

$$\overline{F}_{con} = \frac{1}{x_f - x_i} \int_{x_i}^{x_f} F_{con}(P_{v,min}, x) dx \quad (22)$$

$$\overline{F}_{exp} = \frac{1}{x_f - x_i} \int_{x_i}^{x_f} F_{exp}(P_{p,max}, x) dx \quad (23)$$

The average contraction and expansion forces, $\overline{F}_{con}$ and $\overline{F}_{exp}$, respectively, are determined as the average for the displacement at the absolute maximum pressure, and are expressed as follows — x_i is
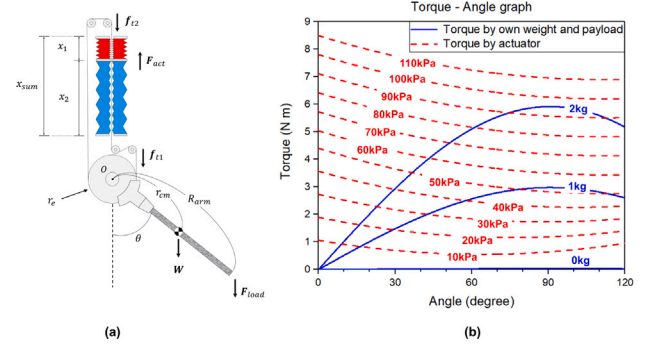
Fig. 7. (a) Variables in CoAM. (b) Torque-angle graph according to actuator and payload.

25 mm, x_f is 125 mm, $P_{v,min}$ is −50 kPa, and $P_{p,max}$ is 60 kPa. The torque that can be generated by each mechanism is as follows.

$$T_{AM} = \frac{D_{act}}{2} \cdot \overline{F}_{con} \quad (24)$$

$$T_{CLM} = \frac{D_{act}}{2} \cdot (\overline{F}_{con} + \overline{F}_{exp}) \quad (25)$$

$$T_{CoAM} = \frac{D_{act}}{2} \cdot (\overline{F}_{con} + \overline{F}_{exp}) \quad (26)$$

In Table 4, it can be seen that AM can use only contraction force, CLM can use force in both directions (but it occupies the largest space), and CoAM uses force in both directions and occupies the smallest space. When compared numerically through lumped torque density, CoAM is 2.58 times larger than AM, which is the conventional mechanism.

Another notable advantage of CoAM is its inherent adaptability, as depicted in Fig. 6(e). The joint's operation with a single BiPAM ensures redundancy; even if one of the two BiPAMs malfunctions, the other can take over, ensuring continued operation. This redundancy is crucial for practical applications where reliability is paramount. Furthermore, the ability to adjust stiffness by depressurizing both chambers of the DC-BiPAM demonstrates the potential of variable stiffness mechanisms [36, 37]. This feature allows for adaptive interactions with environments and enhances safety during human–robot interactions

3.4. Quasi-static model of CoAM

The motion of the CoAM was analyzed using a quasi-static model. The parameters are shown in Fig. 7(a). When the joint is at rest, the following equation can be obtained by considering that the sum of the torques at O, which is the center of the joint, is zero.

$$\sum T_O = T_{act} - T_w - T_{load} = 0 \quad (27)$$

T_{act} is the torque generated by the actuator, T_w is the torque generated by the self-weight of the forearm including the pulley, and T_{load} is the torque generated by the payload at the end effector of the joint. These torque values can be expressed as follows, by the product of radius and force.

$$r_e(F_{act} - f_t) - r_{cm}W \sin\theta + R_{arm}F_{load}\sin\theta = 0 \quad (28)$$

where F_{act} is the force of the actuator according to the pressure displacement of DC-BiPAM, f_t is the friction force generated by the
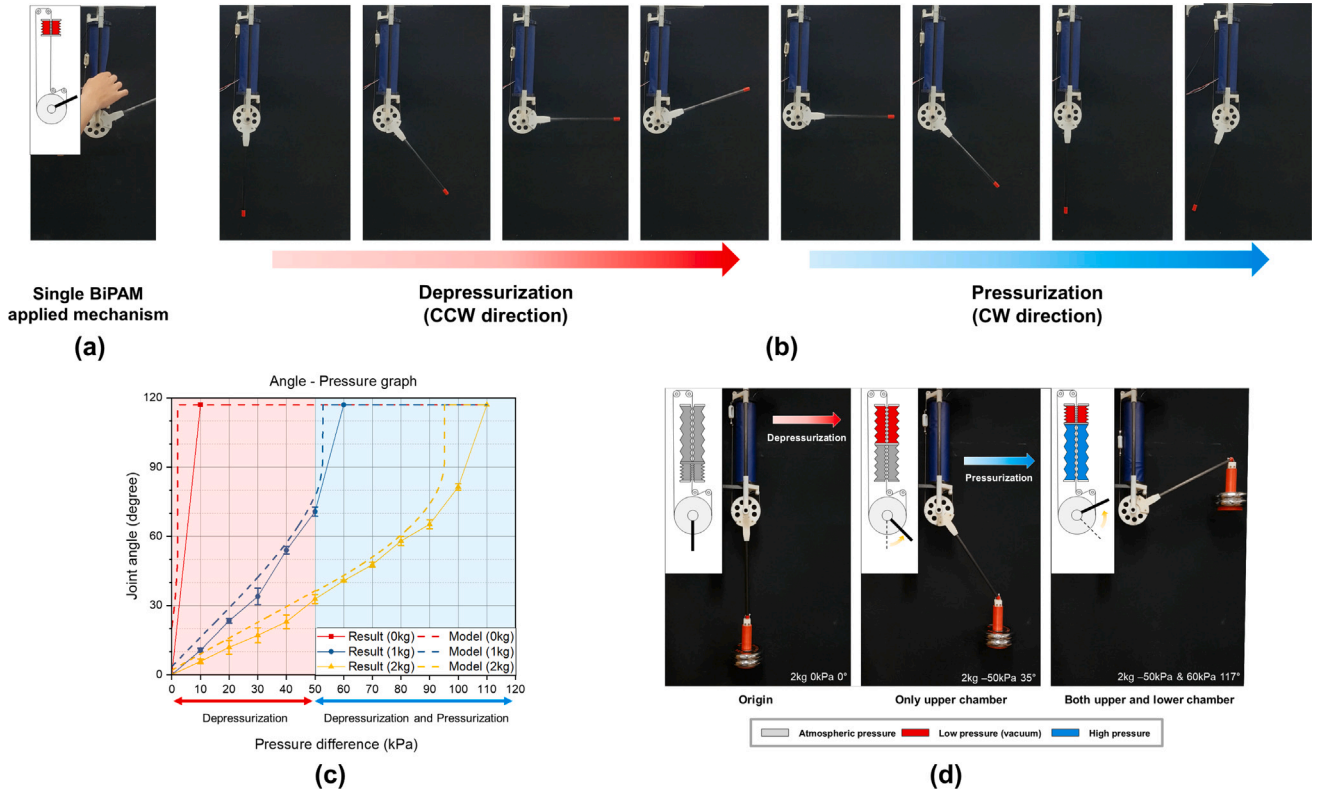
Fig. 8. (a) Bidirectional rotation mechanism with a single BiPAM. (b) Bidirectional movement of the joint according to the internal pressure of a single BiPAM. (c) Angle - Pressure graph of the robot joints according to the actuator pressure difference at different payloads. (d) Process of lifting a 2 kg payload.

bearing and tendon, F_{load} is the weight of the payload applied to the end effector, r_e is the sum of the radius of the joint and tendon, R_{arm} is the length of the forearm, W is the forearm and the pulley's own weigh, r_{cm} is the distance from O to the center of mass, and θ is the rotation angle of the joint. The $r_{cm}W$ was measured using a push-pull gauge at the end effector while maintaining the angle of the joint at $90°$. x_{sum} and x_i were selected. R_{arm} and r_e were selected to make the human arm length and range of motion similar.

$$F_{act} = F_1 + F_2 = F_{con}(P_v, x_1) + F_{exp}(P_p, x_2) \quad (29)$$

The actuator force can be expressed as the sum of the forces generated by the chambers #1 and #2, which can be obtained using Eqs. (16) and (17).

$$x_{sum} = x_1 + x_2 \quad (30)$$

$$x_2 = r_e\theta + x_i = f(\theta) \quad (31)$$

The tendon was configured as a closed loop, and the sum of the displacements of chambers #1 and #2 was always constant. Because the displacement of the actuator corresponds to the length of the arc of the joint, the relationship between the displacement and the angle can be determined.

$$F_{act} = \begin{cases} F_{con}(P_{diff}, x_1) & \text{if } P_{diff} \leq k \\ F_{con}(k, x_1) \\ \quad + F_{exp}(P_{diff} - k, x_2) & \text{otherwise.} \end{cases} \quad (32)$$

$$\text{where } P_{diff} = P_p - P_v, \ P_{v,min} = k$$

Initially, chamber #1 was depressurized to -50 kPa, and chamber #2 was pressurized up to 60 kPa. This simplifies the pressure in each chamber into a single variable, which is the pressure difference P_{diff}. P_p is positive pressure and P_v is negative pressure.

$$f_t = f_{t1} + f_{t2}$$
$$= (1 - e^{\mu(\theta_1 + \theta_2)})F_{act} + (1 - e^{\mu(\theta_3 + \theta_4)})F_{act} \quad (33)$$
$$= (\alpha_{1,2} + \alpha_{3,4})F_{act}$$

f_t can be expressed as above using the coefficient of friction, contact angle, and actuator force. μ is the friction coefficient between the tendon and bearing, and θ_i is the contact angle between the tendon and bearing #i ($i = 1, 2, 3, 4$). In this study, the values that cause the friction and actuator forces to act linearly ($\alpha_{1,2}$ and $\alpha_{3,4}$) are defined and measured [38].

$$F_{act} = \begin{cases} F_{con}(P_{diff}, f(\theta)) & \text{if } P_{diff} \leq k \\ F_{con}(k, f(\theta)) \\ \quad + F_{exp}(P_{diff} - k, x_{sum} - f(\theta)) & \text{otherwise.} \end{cases} \quad (34)$$

Eq. (34) is obtained by substituting Eqs. (31) into (32). This indicates that F_{act} depends on P_{diff} and θ. Thus T_{act} can be expressed as follows.

$$T_{act} = r_e(F_{act}(P_{diff}, \theta) - f_t) \quad (35)$$

The torque generated by the self-weight and payload is defined as $T_{passive}$ and is expressed as follows.

$$T_{passive} = T_w + T_{load} = r_{cm}W \sin\theta + R_{arm}F_{load} \sin\theta \quad (36)$$

Fig. 7(b) shows the angle on the x-axis and the torque value on the y-axis. The dashed line indicates the torque generated by the actuator at each pressure level (Eq. (35)). And the solid lines represent the required torque by the self-weight and payload (Eq. (36)). Eqs. (35) and (36) are calculated with the constants shown in Table 5. The x value at the intersection of the dotted and solid lines represents the predicted value of the joint rotation angle at this pressure. If the dashed line is always above the solid lines, the joint moves to the maximum angle ($117°$).
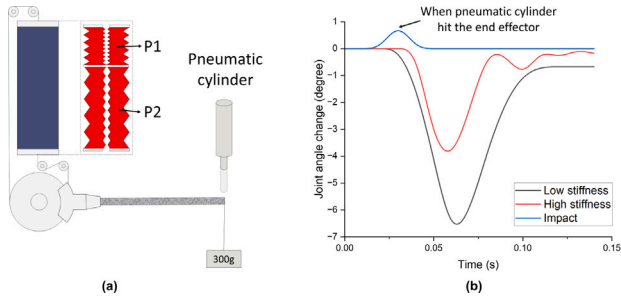
4. Experiment

4.1. Bidirectional rotation with single BiPAM

To show that bidirectional movement is possible with a single BiPAM, the experiment is conducted. In Fig. 8(a), the actuatorless

Table 5
Designed and measured value.

Parameter	Value
r_e	38.6 mm
R_{arm}	300 mm
x_i	20 mm
x_{sum}	120 mm
$P_{v,min}$	50 kPa
$r_{cm}W$	3.60×10^{-3} N · m
$\alpha_{1,2}$	6.8×10^{-2}
$\alpha_{3,4}$	6.6×10^{-2}

Fig. 9. (a) Experimental schematic of stiffness test. (b) Joint angle response of different pressure in DC-BiPAM by the same impact.

section is pressed manually to confirm that there is only one actuator. A red tape is placed on the end effector of the joint. When the actuator is depressurized, CCW rotation is possible from 0–117°, and when the actuator is pressurized, CW rotation is possible from 117° to −15° (Fig. 8(b))

4.2. Payload lifting with DC-BiPAM

To prove the validity of cooperative actuation, the following experiments were conducted. Payload lifting tests were performed by placing 0, 1, and 2 kg weights on the end effector of the robot arm, and changing the actuator's internal pressure to 10 kPa. The *x*-axis of the graph in Fig. 8(c) shows the pressure difference between the chambers #1 and #2, and the *y*-axis shows the angle of the joint. The figure also shows the predictions obtained using the dashed lines. The chamber #1 was depressurized until −50 kPa to create torque in the joint. Then, chamber #2 was pressurized to 60 kPa to create torque in the joint. This implies that the pressure difference of the actuator varied from 0 kPa to 110 kPa. Without a load, the joint moved to 117°, and the maximum angle was attained at 10 kPa. At 1 kg, when the chamber #1 was decompressed to −50 kPa, it moved to 70°. The joint subsequently moved to 117°, which is the maximum angle of the joint, when an additional 10 kPa of pressure was applied. When the load was 2 kg, the joint moved to 35° with −50 kPa decompression and 60 kPa pressurization (Fig. 8(d)).

4.3. Various stiffness of CoAM with DC-BiPAM

The stiffness of the robot joint can be changed by depressurizing both chambers of DC-BiPAM. If the pressure difference between the two chambers is the same, then the robot joint is located at the same position. As shown in Fig. 9(a), 300 g was hung on the end effector of the robot, the pressure of chamber #1 was maintained at P1, and the pressure of chamber #2 at P2. The end effector of the robot was given the same impact through a pneumatic cylinder (CDG1ZA25), and the angle at this time was compared. Table 6 shows the pressure values according to each state, and it can be seen that the angle changes by approximately 7° in the low-stiffness state and the angle changes by approximately 4° in the high-stiffness state (Fig. 9(b)).

Table 6
Designed and measured value.

	P1	P2
Low stiffness	−20 kPa	0 kPa
High stiffness	−40 kPa	−20 kPa

5. Conclusions

In our exploration of soft robotics, the development of a new pneumatic artificial muscle capable of bidirectional force transmission marks a significant advancement. This innovative actuator, along with our cooperative antagonist mechanism, offers improved torque density and functionality over traditional soft actuators like McKibben muscles.

Acknowledging the valuable feedback from our reviewers, we recognize that certain aspects, such as the inclusion of V-bearing #4, warrant further consideration. Initial designs incorporated this component as a critical feature; however, subsequent evaluations suggest that its removal could simplify the design without sacrificing performance.

As we continue to refine our design, the focus will also shift towards enhancing control algorithms for joint position, force, and stiffness. These advancements are essential for the next generation of soft robotic systems. We anticipate that the insights and developments presented in this study will serve as a cornerstone for future innovations in the field.

CRediT authorship contribution statement

Jae Hyeong Park: Conceptualization, Data curation, Methodology, Software, Visualization, Writing – original draft. **Kihyeon Kim:** Conceptualization, Validation, Writing – review & editing. **Young Jin Gong:** Investigation, Writing – review & editing. **Sang Yul Yang:** Investigation. **Seong Taek Hwang:** Investigation. **Ho Sang Jung:** Methodology, Validation. **Hyungpil Moon:** Supervision. **Ja Choon Koo:** Supervision. **Hugo Rodrigue:** Supervision. **Hyouk Ryeol Choi:** Supervision.

Declaration of competing interest

The authors declare that they have no known competing financial interests or personal relationships that could have appeared to influence the work reported in this paper.

Data availability

Data will be made available on request.

Acknowledgments

Appendix A. Supplementary data

Supplementary material related to this article can be found online at https://doi.org/10.1016/j.mechatronics.2023.103099.

References

[1] Haddadin Sami, Albu-Schäffer Alin, Hirzinger Gerd. Safety evaluation of physical human–robot interaction via crash-testing. In: Robotics: Science and systems, vol. 3, Citeseer; 2007, p. 217–24.

[2] Polygerinos Panagiotis, Correll Nikolaus, Morin Stephen A, Mosadegh Bobak, Onal Cagdas D, Petersen Kirstin, et al. Soft robotics: Review of fluid-driven intrinsically soft devices; manufacturing, sensing, control, and applications in human–robot interaction. Adv Energy Mater 2017;19(12):1700016.

[3] El-Atab Nazek, Mishra Rishabh B, Al-Modaf Fhad, Joharji Lana, Alsharif Aljohara A, Alamoudi Haneen, et al. Soft actuators for soft robotic applications: A review. Adv Intell Syst 2020;2(10):2000128.

[4] Rodrigue Hugo, Wang Wei, Han Min-Woo, Kim Thomas JY, Ahn Sung-Hoon. An overview of shape memory alloy-coupled actuators and robots. Soft Robot 2017;4(1):3–15, PMID: 29182099.

[5] Park Seong Jun, Kim Uikyum, Park Cheol Hoon. A novel fabric muscle based on shape memory alloy springs. Soft Robot 2020;7(3):321–31, PMID: 31724903.

[6] Haines Carter S, Lima Márcio D, Li Na, Spinks Geoffrey M, Foroughi Javad, Madden John DW, et al. Artificial muscles from fishing line and sewing thread. Science 2014;343(6173):868–72.

[7] Yip Michael C, Niemeyer Günter. On the control and properties of supercoiled polymer artificial muscles. IEEE Trans Robot 2017;33(3):689–99.

[8] Yang Sang Yul, Cho Kyeong Ho, Kim Youngeun, Song Min-Geun, Jung Ho Sang, Yoo Ji Wang, et al. High performance twisted and coiled soft actuator with spandex fiber for artificial muscles. Smart Mater Struct 2017;26(10):105025.

[9] Kim Kihyeon, Cho Kyeong Ho, Jung Ho Sang, Yang Sang Yul, Kim Youngeun, Park Jae Hyeong, et al. Double helix twisted and coiled soft actuator from spandex and nylon. Adv Energy Mater 2018;20(11):1800536.

[10] Palli Gianluca, Natale Ciro, May Chris, Melchiorri Claudio, Wurtz Thomas. Modeling and control of the twisted string actuation system. IEEE/ASME Trans Mechatronics 2013;18(2):664–73.

[11] Carpi Federico, Rossi Danilo De. Bioinspired actuation of the eyeballs of an android robotic face: Concept and preliminary investigations. Bioinspiration Biomim 2007;2(2):S50.

[12] Jung Ho Sang, Phung Hoa, Park Jae Hyeong, Yang Sang Yul, Kim Kihyeon, Ko Jeong U, et al. Development of a small and lightweight missile fin control actuation system driven by novel dielectric elastomer actuators. IEEE/ASME Trans Mechatronics 2021;26(2):1002–12.

[13] Tondu B, Lopez P. Modeling and control of McKibben artificial muscle robot actuators. IEEE Control Syst Mag 2000;20(2):15–38.

[14] Tondu B, Ippolito S, Guiochet J, Daidie A. A seven-degrees-of-freedom robot-arm driven by pneumatic artificial muscles for humanoid robots. Int J Robot Res 2005;24(4):257–74.

[15] Ohta Preston, Valle Luis, King Jonathan, Low Kevin, Yi Jaehyun, Atkeson Christopher G, et al. Design of a lightweight soft robotic arm using pneumatic artificial muscles and inflatable sleeves. Soft Robot 2018;5(2):204–15, PMID: 29648951.

[16] Li Shuguang, Vogt Daniel M, Rus Daniela, Wood Robert J. Fluid-driven origami-inspired artificial muscles. Proc Natl Acad Sci 2017;114(50):13132–7.

[17] Hawkes Elliot W, Christensen David L, Okamura Allison M. Design and implementation of a 300% strain soft artificial muscle. In: 2016 IEEE international conference on robotics and automation. 2016, p. 4022–9.

[18] Diteesawat Richard Suphapol, Helps Tim, Taghavi Majid, Rossiter Jonathan. Characteristic analysis and design optimization of bubble artificial muscles. Soft Robot 2021;8(2):186–99, PMID: 32552345.

[19] Felt Wyatt, Robertson Matthew A, Paik Jamie. Modeling vacuum bellows soft pneumatic actuators with optimal mechanical performance. In: 2018 IEEE international conference on soft robotics. 2018, p. 534–40.

[20] Oguntosin Victoria, Akindele Ayoola. Design and characterization of artificial muscles from wedge-like pneumatic soft modules. Sensors Actuators A 2019;297:111523.

[21] Lee Jin-Gyu, Rodrigue Hugo. Origami-based vacuum pneumatic artificial muscles with large contraction ratios. Soft Robot 2019;6(1):109–17.

[22] Li Shuguang, Vogt Daniel M, Bartlett Nicholas W, Rus Daniela, Wood Robert J. Tension pistons: Amplifying piston force using fluid-induced tension in flexible materials. Adv Funct Mater 2019;29(30):1901419.

[23] Putzu Fabrizio, Abrar Taqi, Althoefer Kaspar. Plant-inspired soft pneumatic eversion robot. In: 2018 7th IEEE international conference on biomedical robotics and biomechatronics. 2018, p. 1327–32.

[24] Abrar T, Putzu F, Konstantinova J, Althoefer K. EPAM: Eversive pneumatic artificial muscle. In: 2019 2nd IEEE international conference on soft robotics. 2019, p. 19–24.

[25] Oh Namsoo, Park Yeong Jae, Lee Seongbok, Lee Haneol, Rodrigue Hugo. Design of paired pouch motors for robotic applications. Adv Mater Technol 2019;4(1):1800414.

[26] Coad Margaret M, Thomasson Rachel P, Blumenschein Laura H, Usevitch Nathan S, Hawkes Elliot W, Okamura Allison M. Retraction of soft growing robots without buckling. IEEE Robot Autom Lett 2020;5(2):2115–22.

[27] Zhang Jia-Fan, Yang Can-Jun, Chen Ying, Zhang Yu, Dong Yi-Ming. Modeling and control of a curved pneumatic muscle actuator for wearable elbow exoskeleton. Mechatronics 2008;18(8):448–57.

[28] Minh Tri Vo, Kamers Bram, Ramon Herman, Van Brussel Hendrik. Modeling and control of a pneumatic artificial muscle manipulator joint–Part I: Modeling of a pneumatic artificial muscle manipulator joint with accounting for creep effect. Mechatronics 2012;22(7):923–33.

[29] Niiyama Ryuma, Sun Xu, Sung Cynthia, An Byoungkwon, Rus Daniela, Kim Sangbae. Pouch motors: Printable soft actuators integrated with computational design. Soft Robot 2015;2(2):59–70.

[30] Ko Junghyuk, Jun Martin B, Gilardi Gabriele, Haslam Edmund, Park Edward J. Fuzzy PWM-PID control of cocontracting antagonistic shape memory alloy muscle pairs in an artificial finger. Mechatronics 2011;21(7):1190–202.

[31] Feng Yunhao, Ide Tohru, Nabae Hiroyuki, Endo Gen, Sakurai Ryo, Ohno Shingo, et al. Experimental comparison of antagonistic hydraulic muscle actuation under single/dual and zero/overlapped servovalve configurations. Mechatronics 2022;83:102737.

[32] Usevitch Nathan S, Okamura Allison M, Hawkes Elliot W. APAM: Antagonistic pneumatic artificial muscle. In: 2018 IEEE international conference on robotics and automation. 2018, p. 1539–46.

[33] Chen Yinglong, Zhang Junhao, Gong Yongjun. Novel design and modeling of a soft pneumatic actuator based on antagonism mechanism. Actuators 2020;9(4).

[34] Niiyama Ryuma, Sun Xu, Sung Cynthia, An Byoungkwon, Rus Daniela, Kim Sangbae. Pouch motors: Printable soft actuators integrated with computational design. Soft Robot 2015;2(2):59–70.

[35] Goodman AW, Goodman Gary. Generalizations of the theorems of pappus. Amer Math Monthly 1969;76(4):355–66.

[36] Lemerle Simon, Grioli Giorgio, Bicchi Antonio, Catalano Manuel G. A variable stiffness elbow joint for upper limb prosthesis. In: 2019 IEEE/RSJ international conference on intelligent robots and systems. IEEE; 2019, p. 7327–34.

[37] Baggetta Mario, Berselli Giovanni, Palli Gianluca, Melchiorri Claudio. Design, modeling, and control of a variable stiffness elbow joint. Int J Adv Manuf Technol 2022;122(11–12):4437–51.

[38] Reinecke Jens, Chalon Maxime, Friedl Werner, Grebenstein Markus. Guiding effects and friction modeling for tendon driven systems. In: 2014 IEEE international conference on robotics and automation. 2014, p. 6726–32.

Jae Hyeong Park received a B.S. degree in Mechanical Engineering from Sungkyunkwan University, Suwon, 16419, Republic of Korea, in 2017. He is currently pursuing a Ph.D. degree at the School of Mechanical Engineering in the Robotics Innovatory, Sungkyunkwan University, Suwon, Korea. His research interests include soft pneumatic robots and artificial muscles.
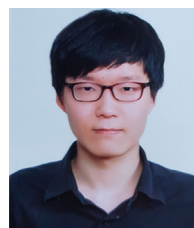
Kihyeon Kim received a B.S. degree in Mechanical Engineering from Sungkyunkwan University, Suwon, 16419, Republic of Korea, in 2017. He is currently pursuing a Ph.D. degree at the School of Mechanical Engineering in the Robotics Innovatory, Sungkyunkwan University, Suwon, Korea. His research interests include soft robotics and artificial muscles.

Young Jin Gong received a B.S. degree in mechanical engineering, in 2020, from Sungkyunkwan University, Suwon, South Korea, where he is currently working toward a Ph.D. degree in soft pneumatic actuators and their applications with the Robotics Innovatory, School of Mechanical Engineering.

Sang Yul Yang received a B.S. and Ph.D. degree in Mechanical Engineering from Sungkyunkwan University, Suwon, 16419, Republic of Korea, in 2016 and 2022. His research interests include soft robotics and artificial muscles.

Seong Tak Hwang received a B.S. and M.S. degree in Mechanical Engineering from Sungkyunkwan University, Suwon, 16419, Republic of Korea, in 2019 and 2021. His research interests include soft robotics and artificial muscles.

Ho Sang Jung received a B.S. and Ph.D. degree in Mechanical Engineering from Sungkyunkwan University, Suwon, 16419, Republic of Korea, in 2013 and 2020. His research interests include soft robotics and artificial muscles.

Hyungpil Moon received the B.S. and M.S. degrees in mechanical engineering from the Pohang University of Science and Technology, Pohang, South Korea, in 1996 and 1998, respectively, and the Ph.D. degree in mechanical engineering from the University of Michigan, Ann Arbor, MI, USA, in 2005. From 2006 to 2007, he was a Postdoctoral Researcher with the Robotics Institute, at Carnegie Mellon University. In 2008, he joined the Faculty of the School of Mechanical Engineering, Sungkyunkwan University, Suwon, South Korea, where he is currently a Professor. His current research interests include robotic manipulation, SLAM, combined task and motion planning, and polymer-based sensor and actuators. He is the Co-Chair for IEEE RAS TC on Robotic Hand, Grasping, and Manipulation. He was a Technical Editor of IEEE/ASME TRANSACTIONS MECHATRONICS and the Editor-in-Chief of the Journal of Korea Robotics Society. He is also serving as an Editor for ICRA, and an Associate Editor for Intelligent Service Robotics.

Ja Choon Koo received a B.S. degree in mechanical engineering from Hanyang University, Seoul, South Korea, and the M.S. and Ph.D. degree in mechanical engineering from the University of Texas at Austin, Austin, TX, USA. He is currently a Professor at the School of Mechanical Engineering, Sungkyunkwan University, Suwon, South Korea. His primary research interests include the field of design, analysis, and control of dynamic systems with an emphasis on mechatronics and robotic applications. Formerly, he was a Research Engineer with IBM, San Jose, CA, USA, and an Engineering Staff Member with SISA, San Jose, CA, USA. He was a Visiting Scholar with the University of California and IBM research.

Hugo Rodrigue received a B.Eng. in Mechanical Engineering from McGill University in Montreal, Canada in 2008, an M.Sc.A. in Industrial Engineering from École Polytechnique de Montréal, Canada in 2010, and a Ph.D. in Mechanical and Aerospace Engineering from Seoul National University of Seoul, Korea in 2015. He has been an Assistant Professor at the School of Mechanical Engineering at Sungkyunkwan University in Suwon, Korea since 2016 where he leads the Soft Robotics Laboratory. His research interests are soft robots and actuators, novel sensors and actuators, and hybrid soft/rigid structures. Prof. Rodrigue is currently serving as the Associate Vice President of the IEEE Robotics and Automation Society Technical Activities Board. He is an Associate Editor for IEEE Robotics and Automation Letters and for the Journal of Intelligent Service Robotics. He served as an Associate Editor of the IEEE International Conference on Robotics and Automation (ICRA) in 2022 and as publicity chair of the IEEE International Conference on Soft Robotics (RoboSoft) 2019.

Hyouk Ryeol Choi received the B.S. degree from Seoul National University, Seoul, Korea, the M.S. degree from the Korea Advanced Institute of Science and Technology, Daejeon, Korea, and the Ph.D. degree from Pohang University of Science and Technology, Pohang, Korea, in 1984, 1986, and 1994, respectively, all in mechanical engineering. From 1986 to 1989, he was an Associate Research Engineer with the IT Research Center, LG Electronics. From 1993 to 1995, he was a Postdoctoral Researcher at Kyoto University, Kyoto, Japan. From 1999 to 2000, he visited the National Institute of Advanced Industrial Science and Technology, Japan as a JSPS Fellow. From 2008 to 2009, he was a Visiting Professor at the University of Washington, Seattle, USA. Since 1995, he has been a Professor at the School of Mechanical Engineering, Sungkyunkwan University, Suwon, South Korea.

His research interests include soft robotics, robotic mechanisms, field applications of robots, dexterous robotic hands, and manipulation. Prof. Choi was an Associate Editor of the IEEE Transactions on Robotics, Technical Editor of the IEEE/ASME TRANSACTIONS ON MECHATRONICS, and the Senior Editor of the Journal of Intelligent Service Robotics. He was a founding co-chair of the IEEE RAS technical committee Robot Hand, Grasping and Manipulation. He was the General Chair of the 2012 IEEE Conference on Automation Science and Engineering(CASE), in Seoul, Korea.